Accepted Manuscript

Temperature control synthesis of platinum nanoparticle-decorated reduced graphene oxide of different functionalities for anode-catalytic oxidation of methanol

Senjuti Banik, Ankita Mahajan, Apurba Ray, Dipanwita Majumdar, Sachindranath Das, Swapan Kumar Bhattacharya
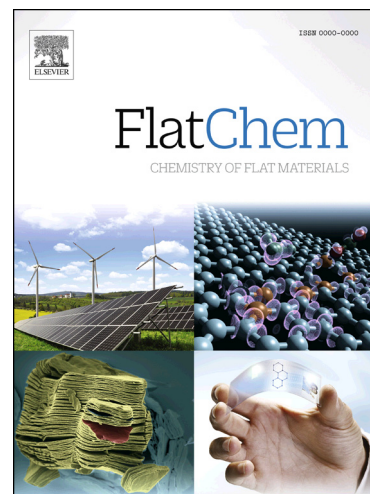
Please cite this article as: S. Banik, A. Mahajan, A. Ray, D. Majumdar, S. Das, S. Kumar Bhattacharya, Temperature control synthesis of platinum nanoparticle-decorated reduced graphene oxide of different functionalities for anode-catalytic oxidation of methanol, *FlatChem* (2019), doi: https://doi.org/10.1016/j.flatc.2019.100111

Temperature control synthesis of platinum nanoparticle-decorated reduced graphene oxide of different functionalities for anode-catalytic oxidation of methanol

Senjuti Banik[1], Ankita Mahajan[1], Apurba Ray[2], Dipanwita Majumdar[3], Sachindranath Das[2], Swapan Kumar Bhattacharya[1]*

[1]Physical Chemistry Section, Department of Chemistry, Jadavpur University, Kolkata 700032, India

[2]Department of Instrumentation Science, Jadavpur University, Kolkata 700032, India

[3]Department of Chemistry, Chandernagore College, Chandannagar, Hooghly, WB-712136, India

*Corresponding author's address: Email – skbhatt7@yahoo.co.in,

Tel.: +919831699643,

Fax: +913324146584.

Abstract

Platinum (Pt) nanoparticles of varying average diameters decorated on exfoliated reduced graphene oxide (Pt/rGO) of various functionalities have been synthesized by monitoring the temperature of co-reduction of Pt^{IV} and GO. The as-synthesized composites are characterized by X-ray diffraction, spectroscopic, thermo gravimetric and microscopic studies. The excellent catalytic capability of the composites for methanol oxidation reaction (MOR) is found to be synergistic in reference to single components, Pt and rGO and might be used in high efficient, less emissive, cost-effective direct methanol fuel cell operated in alkali. The poison tolerance capability of the electrodes as measured by the ratio of forward and backward peak currents due to MOR is found to be relatively high in respect to similar data in the literature and increases with the increase of defect concentration as evaluated from Raman spectroscopic study, on rising the temperature of synthesis of the catalyst. The forward peak current density of the electrode made with Pt/rGO composite synthesized at 40ºC is greater by 5.6 and 287 times than these for pure Pt and rGO based electrodes. The electrode exhibits the best catalytic activity due to presence of the lowest but sufficient defect sites, especially for formation of sp^2-C-OH groups on the rGO surface in the vicinity of the poisoned Pt-surface and lowest average diameter (7.41 nm) of dispersed Pt nanoparticles.

Keywords: *Platinum (Pt) nanoparticle-decorated reduced graphene oxide, methanol oxidation, oxygen functionalities, defects concentration, temperature controlled-synthesis*

1. Introduction

Ever-rising demand for environmental benign sustainable energy sources has driven immense attention to direct methanol fuel cells (DMFCs), particularly for application in transportation and portable energy devices [1, 2]. Methanol being a single carbon containing liquid fuel is well-studied for its simple structure, low production cost, high abundance, processability and portability [3, 4]. It is inherently less prone to ignition and has high volumetric energy density (15.6 MJ/L) compared to di-hydrogen (1.91 MJL^{-1} at 20 mPa). Moreover, it is toxic if ingested but non-hazardous in presence of reasonable safety precautions. In addition, it is stable, less volatile, and remains in liquid phase over a wide temperature range, embracing all operational criteria for fuel cells, and hence widely employed in renewable energy generation technology [5].

Platinum (Pt) is considered as one of the efficient electrocatalysts for DMFCs. However, the high fabrication prices and low stability inhibit commercial applications of common Pt-based catalysts [6]. It is eminent that the electrocatalytic performance of a fuel cell depends highly on the composition, size, morphology and dispersion of the catalytic nano-phase [7]. The size of Pt nanoparticles is one of the most key factors influencing the performance of the catalyst [8]. Downsizing Pt nanoparticles has been identified as a profitable approach to combat the problem of low efficiency and high production cost of catalysts [9, 10]. However, too small nanostructures due to large surface energy may undergo severe aggregation and adsorption [11, 12] thereby inducing serious declination in their catalytic performance.

An effective strategy for solving these deactivation problems involves uniform loading of the Pt nanoparticle catalysts onto a carrier with a large surface exposure and high electrical

conductivity [13, 14]. Thus the support materials of catalyst play a vital role in controlling these properties. In the recent years significant research has been carried out with various carbon forms such as carbon nano tube (CNT)s, amorphous carbons, polymers as supports for the development of suitable catalyst for direct methanol fuel cells (DMFCs) [15-18]. However, during fuel cell operation, a gradual oxidation of the carbon support leads to detachment of the platinum nanostructures from the carbon support, allowing no improvement to the addressed problems [19, 20] in the long run.

In the last decade, graphene, owing to its unique 2D-morphological and superior electronic properties including low density, high thermal conductivity (5300 $Wm^{-1}K^{-1}$), excellent mechanical flexibility (Young's modulus~1100 GPa), charge transport characteristics (~2000 Scm^{-1}), large surface area (~2630 m^2g^{-1}), have dominated several technological fields of photovoltaics, sensors, drug detection, catalysis, supercapacitors, batteries, fuel cells, allied energy storages, transistors and various optoelectronic devices [21-34]. However single-layered graphenes are quite expensive to fabricate. But recent observations on comparative studies of mono-, few- and multi-layered graphenes for enzyme-immobilization, bio-sensing applications and electrochemical investigations reveal that the results vary little with the number of stacked layers of graphene [35-38]. Thus, less expensive synthetic methods can be adopted for obtaining functionalized multi-layered graphenes which have emerged as the noble material for a variety of different desired investigations. Chemical functionalization of the graphene sheets promotes homogeneous distribution of Pt nanoparticles on its surface. Currently this is achieved by introducing acid oxidation, derivatization using simple ligands, ionic liquids, conductive polymers, and similar other systems [39-42]. Graphite on oxidative exfoliation forms graphene oxide with abundant oxygen-containing functional groups on the surfaces that can be used as

anchoring sites for metal nanoparticles. However, poor charge transport limits its usage and hence combination of reduced graphene oxide with functional Pt nanoparticles in the form of composites may lead to interesting materials with enhanced electrocatalytic activities [43-57]. Many studies have been reported on the performances of Pt/graphene composites for electrocatalytic DMFCs, (**Table S1**) but these studies are made from the aspects of material improvement and lack physicochemical and electrochemical co-relation and analysis in detail with respect to the defects, dimension, capacity contribution, etc. Moreover, other major problems in this research field are still to be addressed. Firstly, most of the electro-catalysis is carried out in acid instead of alkaline media but disposal of the electrolytes after completion of lifetime and corrosion are big environmental issues! Secondly, Pt/rGO catalysts exhibited better CO tolerance in alkaline media, which increases the catalytic efficiency. Thirdly, the stability of the composite catalysts needs to be improved for commercialization purposes. Fourthly, in numerous studies the composite catalysts require polymer binders and conductive additives for modifying the surfaces of carbon electrodes for catalyzing methanol oxidation. However, such modifications result in less efficiency of Pt nanoparticles as only a fraction of Pt nanoparticles available on the surfaces of composite films gets chance to participate in electrocatalytic processes [11, 12]. Last but not the least, among the various methods available in the literature, chemical reduction (using reductants like sodium borohydrides, hydrazine, H_2O_2, citrates, etc.) followed by thermal treatment has been the most popular, facile, cost-effective and convenient technique for obtaining functionalized-graphene decorated with Pt nanoparticles [58-59]. However, the optimization of temperature of synthesis is very essential to tune the presence of oxygen-functionalities on rGO surface as well as reduce Pt in presence of chemical reductants. Such oxygen functionalities have significant influence in CO

tolerance behavior during electrocatalysis of methanol oxidation. However, few studies are available in the literature [60] in this regard. In the present work, we report systematic study of electrocatalytic oxidation of methanol using Pt/rGO composites synthesized at different temperatures to optimize the aforesaid problems. The as synthesized catalyst materials have been characterized using Fourier Transform Infrared Spectroscopy (FTIR), Raman spectroscopy, Thermo Gravimetric Analysis (TGA) and X-ray Photoelectron Spectroscopy (XPS) to get detail idea about its chemical distinctiveness. Powder X-ray Diffraction (PXRD), Field Emission Scanning Electron Microscopy (FESEM) analysis, High Resolution Transmission Electron Microscopy (HRTEM) techniques are used for crystallinity and morphological studies while the electrochemical characterizations have been carried out using cyclic voltammetry, chronoamperometry and electrochemical impedance spectroscopy.

2. Experiments

2.1. Chemicals

All chemicals were purchased from Merck (India) and used without further purification. Milli-Q water was used to make all solutions. All the glass apparatus were properly cleaned with chromic acid and then rinsed with Millipore water.

2.2. Synthesis of catalyst

The synthesis of GO supported Pt nanoparticles, was carried out in one pot by chemical reduction of GO sheet embedded with K_2PtCl_6 by hydrazine at different temperatures. GO was first prepared from fine graphite powder by using modified Hummer's method reported elsewhere [61]. Then, typically, 2.81 mL of 0.02 M of K_2PtCl_6 (0.01 g Pt) solution was added into 20 mL aqueous dispersion of 0.1 g GO taken in a beaker and adsorbed by ultrasonication for 1 h. After that, excessive hydrazine solution was added slowly under continuous stirring at room temperature (28ºC). The resulting black coloured precipitate was collected by centrifugation, washed with excess distilled water and finally dried in vacuum desiccators at room temperature. The coloured powder obtained is denoted as Pt/rGO-28. Other catalyst-samples were also synthesized by the similar procedure at varied temperature of 40ºC, 60ºC, and 80ºC and are marked as Pt/rGO-40, Pt/rGO-60, Pt/rGO-80 respectively. In order to compare these supported Pt catalysts with bare one, Pt nano-catalyst was synthesized at room temperature using the same procedure barring addition of GO.

2.3. Physical and electrochemical characterization

The XRD of all samples were conducted using a Philips 1710, USA X-ray diffractometer provided with a source of Cu Kα radiation (α= 0.1541 Å). The morphological investigations were done using scanning electron microscopy (SEM, SUPRA 55 VP-41-32 instrument with the smart SEM version 5.05 Zeiss software), HRTEM (JEOL JEM-2000E7) and XPS (PHI 5000 Versa probe II, ULVAC-PHI, INC., USA using monochromatic Al Kα X-ray source (1486.6 eV)). Raman spectra were carried out in solid state using 514 nm laser excitation using model T64000 (Make Jobin Yvon Horiba, France), Argon-Krypton mixed ion gas laser of model 2018 RM (Make Spectra Physics, USA) as excitation source, optical microscope of model BX41 (Make Olympus, Japan) as collection optic system and thermoelectric cooled front illuminated 1024 256 CCD., model Synpse TM (Make Jobin Yvon Horiba, France) detector.

The synthesized catalysts and GO were also characterized by the FTIR (perkin Elmer, Spectrum RX1, resolution 4cm^{-1}). The electrochemical properties of all the catalysts were measured at room temperature using the instruments and procedures previously described [62]. A computer aided Potentiostat/Galvanostat (AEW-2, Munistst, Sycopel Scientific Ltd, UK) was connected with a two compartment glass cell fitted with a conventional three electrode assembly containing a graphite rod (geometrical surface area 0.24 cm^2) covered with a prepared catalyst, a Pt foil (1 cm $\times$ 1 cm) and and Hg/HgO/OH$^-$ (0.1 M) electrode (MMO) (0.1 V relative to standard hydrogen electrode, SHE) as working, counter, and reference electrodes, respectively. Cyclic voltammetry (CV) studies were carried out in 1 M NaOH solution with and without methanol of strength 0.5 M in the potential range of -0.9 V to +0.6 V at different scan rates. Nyquist profiles were also recorded by applying a fixed potential of -0.1 V. All cyclic voltammograms were recorded when almost steady profiles were obtained. Amperometric i–t curves were recorded at

an initial potential of (-0.2V). Polarization data were collected by potentiodynamic method using a scan rate of $1mVs^{-1}$. So, Tafel slopes and equilibrium exchange current densities are only apparent in nature. Electrochemical impedance spectroscopy (EIS) measurements (CS313, CorrTest china) were conducted at a fixed potential (-100mV) in the frequency range from 100 kHz to 0.01 Hz.

3. Results and discussion

3.1. Structural characterizations

3.1.1. Powder X-ray Diffraction (PXRD)

Figure 1a shows the PXRD patterns of collected graphite powder and as synthesized GO. The X-ray peak of the graphite powder is observed at 2θ value of 26.6º for characteristic (002) plane indicating an average interlayer distance of 0.337 nm, which on oxidation shifts to 10.2º indicating that the interlayer distance in the synthesized GO increases to 0.709 nm [63]. This indicates exfoliation of graphite through formation of oxygenated functional groups e.g epoxide, carbonyl, carboxyl etc, and incorporation of water molecules in the layers of the graphene sheets. Moreover, the presence of these functional groups makes graphene oxide hydrophilic. These oxygen-containing functional groups also act as anchoring sites for metal complexes [64]. **Figure 1b** shows PXRD of Pt/rGO catalysts synthesized at different temperatures. The strong characteristic diffraction peaks at 2θ = 39.8º, 46.3º, 67.7º and 81.4º can be assigned respectively to (111), (200), (220) and (311) planes of synthesized Pt nanoparticle of face-centered-cubic (fcc) crystal structure (JCPDS # 870646) developed on rGO surface. Moreover, peak around 2θ value of 28.4º signifies (200) plane of body centred cubic crystal of Pt_3O_4 (JCPDS # 741870). The relative peak intensity of (200) plane of Pt_3O_4 in reference to that of (111) plane decreases

9

gradually in the order from 0.66 (for Pt/rGO-28) to 0.09 as the rate of metal reduction along with the other reaction increases on increasing temperature from 28º C to 80º C. This signifies that insignificant amount of Pt_3O_4 is produced particularly when the reducing environment becomes more drastic at the higher temperature. It is also noted that the as-synthesized Pt/rGO composites show broad peaks characteristic of rGO samples. The 2θ values of (002) plane appear around 25.5º as presented by the magnified selected portion of the profile of Pt/rGO-40 at the inset. This feature is attributed to random stacking of crimped graphene sheets obtained through in-situ chemical reduction of GO. Furthermore, the average sizes (τ) of the crystalline domains of the Pt nanoparticles in the composite samples are calculated on the basis of full width at half maximum **(FWHM)** of some prominent diffraction peaks. Since different diffraction peaks are slightly shifted from the unsupported Pt catalyst (see supplementary **Figure. S1**) and the corresponding JCPDS data of pure Pt, the existence of micro-strain is expected to be present due to generation of several defects like voids, point defects, line defects, dislocation, etc. The peak broadening therefore may be due to both formation of nanoparticle and micro-strain present in the material. So, Williamson-Hall equation instead of usual Debye Scherrer equation is used to determine the size of the crystallite (**τ**) and microstrain (ε) (see Supplementary). According to Williamson-Hall equation [65]

$$\frac{\beta \cos\theta}{\lambda} = \frac{K}{\tau} + \frac{4\varepsilon \sin\theta}{\lambda}$$

The crystalline size (**τ**) and the microstrain (ε) of Pt/rGO nanocomposites have been calculated from the intercepts and the slopes of βcosθ/λ vs sinθ/λ plots as shown in **Fig. S2**.

Table 1 reveals that the average radius of the crystallites obtained from Williamson-Hall method is gradually decreased on increasing the temperature of synthesis of the catalysts. At high temperature, the rate of nucleation is large. So, smaller crystallites are obtained. The table also

reveals that the size from FESEM is only slightly increased than that obtained from Williamson-Hall method for each of Pt/rGO-28 and Pt/rGO-40 catalysts. But the size obtained from FESEM is greater than that obtained from Williamson-Hall method for the catalysts which were synthesized at higher temperature like 60ºC and 80ºC. This might be due to the significant number of collisions of Pt crystallites at higher temperature, causing agglomeration. Secondly, smaller the crystallites, greater is the surface energy and hence their tendency to agglomerate. Here, large surface energy for samples like Pt/rGO-60 and Pt/rGO-80 causes agglomeration of the crystallites to produce nanoparticles of relatively greater atomic radius as evident from FESEM study. Thirdly, the nanoparticle (Pt) - stabilizer (rGO) interaction will be less for particles synthesized at higher temperature due to higher mobility of atoms and molecules, causing agglomeration. The table also reveals that micro-strain (ε) is negative for Pt/rGO-40 and Pt/rGO-80 indicating lattice shrinkage in conformation with the obtained lattice parameters for the samples. Thus, synthesized small-sized Pt nano particles anchored onto rGO brings out the possibility of enhanced efficiency for alcohol electro-oxidation reactions.

3.1.2. Field Emission Scanning Electron Microscopy (FESEM) analysis

The morphology of as-synthesized materials was characterized by FESEM. **Figure 2a** shows agglomeration of the exfoliated platelets of reduced graphene oxide (rGO) obtained by hydrazine reduction of GO in absence of Pt. The platelets (sheets) are three dimensional in shape, unsymmetrical and randomly dispersed in nature. The surface of the aggregated sheets is fairly smooth due to absence of any anchoring nanoparticles. The multi-layered structure can be understood at the edge of the agglomerates. The stacking of layered structure may be due to strong hydrogen bonding interactions between the rGO layers. **Figure 2b** illustrates deposition of Pt nanoparticles

11

on different layers of reduced graphene oxide synthesized at 40°C. On the other hand, each of **Figure 2c-f** corresponding to Pt/rGO composites synthesized at various temperatures depicts Pt nanoparticle decorated rGO sheets where the size and morphology of deposited Pt are comparable.

The sheets in each sample hold small and low poly-dispersed global Pt nanoparticles distributed throughout the surface. Among the various compositions, the Pt/rGO-40 displays uniformly anchored almost separated Pt nanoparticles of average diameter of 7.41 nm. The average diameters of the Pt nanoparticles are obtained from particle distribution histogram presented at the inset of the corresponding SEM micrograph. The synthesized composites are found to follow the sequence according to their diameter (presented in the parenthesis in nm): Pt/rGO-40 (7.41) < Pt/rGO-28 (8.41) < Pt/rGO-60 (14.85) < Pt/rGO-80 (15.87). The smallest diameter and homogeneity in morphology of Pt nanoparticles for Pt/rGO-40 announces its potentiality for utmost electrocatalytic efficiency in alcohol oxidation reaction.

3.1.3. Transmission Electron Microscopy (TEM)

TEM image of Pt/rGO-40 sample (**Figure 3a**) clearly indicates anchoring of Pt nanoparticles on the surface of ultrathin rGO sheets. The enhanced Pt dispersion on Pt/rGO composite has been further confirmed from the TEM image of Pt nanoparticles prepared without the support of GO where large-sized Pt nanoparticles are obtained in random agglomerated forms (**Figure 3b**). The high-resolution TEM image (**Figure 3c**) of Pt/rGO-40 composite also demonstrates clear lattice fringes with inter-lattice spacing of 0.24 nm corresponding to Pt (111) in good agreement with that observed in the XRD study. **Figure 3d** displays the representative energy dispersive X-ray spectrum of Pt/RGO-40. EDX elemental analysis clearly confirms the presence of platinum,

12

carbon and oxygen only. The absence of other elements in EDX confirms the purity of the sample.

3.1.4. X-ray Photoelectron Spectroscopy (XPS) characterization

In order to achieve more information about the elemental composition and chemical states of the Pt/rGO architecture XPS analysis was done. As presented in **Figure 4a** the survey XPS spectrum of Pt/rGO-40 sample displayed three predominant peaks, namely the Pt 4f peak at around 70.21 eV, C 1s peak at around 283.3 eV, and O 1s peak at around 531.5 eV. There are also two additional peaks for Si 2p and Si 2s at around 100 eV and 162 eV respectively originating from the glass substrate employed for XPS studies. From the calculation of the areas under the curve for Pt and C, it is evident that the ratio of Pt : C = 1:6, which indicates the approximate loading of catalyst on rGO substrate.

The spectrum of Pt 4f in **Figure 4b** could be deconvoluted into six peaks, the two most intense peaks at the binding energies of 70.8 eV and 74.07 eV corresponding to Pt^0 $4f_{7/2}$ and Pt^0 $4f_{5/2}$ [50], and the other two weaker doublets at 72.1 eV, 75.1 eV and 72.7 eV, 76.5 eV are ascribed to Pt^{2+} and Pt^{4+} with the contents of ~20% and ~8%, respectively, signifying that Pt nanoparticles on the rGO were mostly in metallic state. However the peaks get shifted towards lower binding energy indicating easy charge transfer of surface defects sites on reduced graphene oxide [66]. As shown in **Figure 4c**, the O1s spectrum consists one prominent peak for O-C at binding energy 530.8 eV and two less prominent peaks at O=C (532.6 eV) and O-C=O (533.8 eV). This observation confirms reduction of GO to rGO, in agreement with FTIR results. The deconvoluted C1s spectrum in **Figure 4d** illustrates strong peak at 284.5 eV with shoulder at 285.5 eV, ascribed to sp^2 and sp^3 hybridized carbon respectively [42, 43]. The peaks at 286.6 eV is attributed to hydroxyl groups and contributions of carbonyl/quinine respectively, while less

13

intense peaks at 288.4 eV typically observed for rGO come as π–π* peak as a result of restoration of sp^2 carbon network. The peak for carboxyl/ carbonyl groups around 288.9 eV is virtually absent signifying complete chemical reduction of GO. Thus the above study confers two important conclusions: i) relative poor intensities corresponding to oxidized carbon in the composite sample indicate that GO has been effectively reduced to rGO and ii) the presence of Pt nanometals anchored onto rGO sheets.

3.1.5. Fourier Transform Infrared (FTIR) study

 GO exhibits one very broad peak centred around 3348 cm^{-1} with a hump at about 3588 cm^{-1} which is attributed to the hydrogen bonded -OH groups as well as free -OH groups of the carboxylic group and alcoholic -OH functionalities of graphene oxide (**Figure 5**). There are several intense peaks identified at 1725 cm^{-1} (C=O carboxyl or carbonyl stretching vibrations), 1611 cm^{-1} (stretching of C=O conjugated with C=C), 1408 cm^{-1} (sp^2-C-OH as well as C-H bending deformation with aromatic skeletal vibration), 1220 cm^{-1} (C-O-C stretching) and 1160 cm^{-1} (sp^3-C-OH stretching) respectively indicating the presence of various oxygen containing functional groups on GO surface in agreement with previous reports. The Pt/rGO composites exhibit significant differences in their spectra (**Table S2**). Firstly, the O–H vibrations diminished markedly with >C=O and C–O–C stretches almost disappeared, signifying effective removals of these functional moieties from the GO surfaces. Secondly, observation of new peaks around 2900 cm^{-1} and 2650 cm^{-1} attributed to –CH$_2$ stretching indicate formation of C-H bonds especially at the edges of GO during reduction to rGO. Thirdly, overall decrease in epoxy group distribution revealed from diminution in the relative intensity ratio of $v_{c\text{-}o\text{-}c}/v_{c=c}$ and $v_{c\text{-}o\text{-}c}/v_{c=o}$ as temperature of reaction is increased demonstrating chemical reduction of GO to rGO. Further, red shift in the C=O stretching is attributed to chemical interaction of rGO surface with Pt metal nanoparticles

as revealed from earlier studies. Details study shows that the relative ratio of $(OD_{C=C/C=O})$ in **Table 2** is optimum in Pt/rGO-40 signifying maximum restoration of sp^2 carbon-network on graphene oxide surface on account of removal of epoxy and carboxylic acid functional groups through hydrazine reduction compared to other Pt/rGO samples. The unusual higher ratio in GO may be due to overlapping of the C=O, conjugated with C=C and C=C aromatic skeletal vibrations.

Further to note that, the graphite sheets on chemical oxidation get cleaved into smaller fragments held together by epoxy linkages [67]. On hydrazine-reduction, these epoxy-linkages further get converted to sp^2C - OH. Hence smaller rGO fragments with surface–edges functionalized with sp^2C - OH results [68]. Thus, the relative optical density ratio $(OD_{\frac{sp^2C-OH}{C-O-C}})$ is found to vary in the order: GO < Pt/rGO-28 < Pt/rGO-40 < Pt/rGO-60 < Pt/rGO-80 which signifies that greater proportion of $sp^2C - OH$ group formation in rGO than GO and Pt/rGO composites synthesized at higher temperature compare to that at lower temperature. Accordingly, the above studies assertively suggest the formation of Pt/rGO composite with more hydroxyl groups than in GO.

3.1.6. Raman spectroscopic study.

Raman spectroscopy is an effective probe for investigating the structural variations that occur in carbonaceous materials. Typical graphene materials show 2 characteristic bands- G and D respectively. The G band arises as a result of in-plane bond-stretching motion of pairs of sp^2 carbon atoms that constitutes the graphene sheet while the D band occurs from ring breathing mode of sp^2 carbon rings adjacent to a graphene edge or a defect respectively [69]. It is worth noting from **Figure 6a** that the G band gets blue shifted from 1580 cm^{-1} (reported for graphene) to 1594 cm^{-1} in GO sample, which is an indication of a better exfoliation of the graphene layers

through incorporation of defects by introducing epoxy, hydroxyl as well as carboxylic acid groups on oxidation while its red shift in the Pt/rGO samples indicates aggregation of graphene layers through removal of these epoxy as well as carboxylic acid groups due to chemical reduction by hydrazine [70]. Moreover, the relative variations in the intensity ratios (I_D/I_G) for various samples have been compared and the values are given in **Table 3**. An increase in the (I_D/I_G) ratio generally results from: (i) increase in defect states caused by overlap of the G band with the D band (ii) reduction in the number of sheets in rGO compared to graphite and (iii) isolated double bonds separated by functional groups [71]. In order to determine the average size of the sp^2 clusters in GO and the composites, we employed the Tuinstra and Koenig relation, which relates the ratio of D and G peak into the crystallite size as follows: [72]

$$I(\mathbf{D})/I(\mathbf{G}) = C(\lambda)/(L_{\mathbf{a}})^2,$$

where $I(D)$ is the intensity of the D peak, $I(G)$ is the intensity of the G peak, $C(\lambda)$ is the wavelength dependent prefactor = 102 nm^2 for λ = 514 nm and L_a is the average crystallite size of sp^2 domains respectively. Thus, the corresponding L_a values for GO and Pt/rGO - 28/40/80 samples stands as 10 nm, 9.36 nm, 9.51nm and 9.38 nm respectively. The observed decrease in average size of sp^2 clusters in the composites compared to GO is due to the formation of new sp^2 clusters with smaller size [73]. Thus, increasing the reaction temperature accelerates the degree of chemical reduction of GO in the composites thereby improving the average size of sp^2 clusters. However, formation of large Pt nanoparticles anchored to rGO sheets sample again disrupts the above trend. It is further reported that pristine single-layer graphene, shows a single symmetrical sharp 2D peak at ~2690 cm^{-1} while less pronounced broad humps designate multi-layered graphene system. Thus, very broad 2D hump in our composite sample ensures presence of multi-layered structure of graphene which is also supported by morphological studies. The

ratio I_{2D}/I_G is a measure of relative thickness/number of layers present in the composite [74]. Thus we observe that increase in temperature of synthesis leads to better exfoliation of rGO sheets in the corresponding systems. Now higher defect states increase the tolerance capability. Low defect states ensure superior charge transport characteristics in graphene systems and hence better electrocatalytic signature. So, sufficient $sp^2C - OH$ with less defect concentration is required as observed for Pt/rGO-40 sample which demonstrates better performance potentiality for alcohol electro-oxidation reaction.

3.1.7. Thermo Gravimetric Analysis (TGA)

The thermal stability of GO and Pt/rGO were investigated by thermogravimetric analysis (TGA-DTA) in dry air. The TGA analysis shown in **Figure 6b** displays the weight loss of the samples (traces a and b in **Figure 6b**) and the corresponding derivative of the weight loss with respect to temperature (DTA) (traces a′ and b′ in **Figure 6b**). For GO sample, the small derivative peaks seen at temperatures below 100 °C correspond to loss of physically adsorbed water in these two samples [75]. The major mass loss for GO occurs at ~ 150 - 300°C presumably due to pyrolysis of labile oxygen bearing functional groups, yielding subsequently CO, CO_2 and water vapour [76]. A further mass loss occurs at ~ 500°C is attributed to carbonization of the graphene oxide. On the other hand, in the Pt/rGO-40 sample, absence of the thermally labile oxygen functional groups during composite formation results in much increased thermal stability and insignificant mass loss below ~ 400 °C. However, due to chemical exfoliation and reduction in the average graphene sheet size, the final degradation of carbon skeleton in the Pt/rGO composite starts well ahead compared to GO, typical features observed for composite fabrication under similar instances. Thus composite formation in the present case is affirmed from the above studies and the resultant composite is well suited for application in elevated temperature electrocatalytic fuel cells.

3.2. Formation mechanism of Pt/rGO composite

At low temperature, the kinetics of Pt(IV) reduction by hydrazine to Pt(0) is faster in comparison to reduction of GO to rGO by hydrazine but as the reaction temperature increases, the reduction kinetics of GO becomes prominent. This is indicated by the decrease in relative intensity ratio of $\upsilon_{c-o-c}/\upsilon_{c=c}$ and $\upsilon_{c-o-c}/\upsilon_{c=o}$ while increase in the relative intensity ratio of $\upsilon_{c=c}/\upsilon_{c=o}$ as revealed from **Table 2**. So, at low temperature, when the rate of rGO formation is slow, Pt^{4+} (from K_2PtCl_6) counters considerable density of oxygen functionalities on graphene surface to enable its attachment to them. Thus, Pt nanoparticles get anchored onto the surface via oxygen containing groups and we obtain Pt/rGO samples. But as the reaction temperature is increased, the rate of GO reduction by hydrazine increases significantly and competes with of Pt (IV) reduction kinetics. As a consequence, the number of oxygen functionalities (especially -COOH, epoxy groups) on the GO surface now diminishes abruptly on account of its reduction by hydrazine to rGO. The effect is that it reduces the effective number of nucleation sites for Pt to get anchored onto graphene surface. Accordingly such smaller number of nucleation sites leads to agglomeration of Pt-nanoparticles resulting in increasing the nanoparticles size and this also increases the defect on the graphene surface as demonstrated by the relative decrease in the relative intensity ratio of $\upsilon_{c=c}/\upsilon_{c=o}$ observed in **Table 2**. Moreover, such size enhancement of Pt nanoparticles anchored on rGO, also leads to widening of interlayer distance between graphene sheets, leading to better exfoliation as observed for the I_{2D}/I_G values of Raman studies.

18

3.3. Electrochemical Characterization of Pt/rGO nano-composites

3.3.1. Cyclic Voltammetry study

To evaluate the electrochemical activity of all sets of Pt/rGO NPs, cyclic voltammogram (CV) experiments were done within a potential range from -0.9 V to +0.6 V at a scan rate of 50 mV s^{-1} in 1M NaOH solution. For pure Pt electrode in absence of rGO two forward current peaks besides the pair of peaks for dehydrogenation, are found at ca -0.148 V and 0.01 V due to formation of PtOH and PtO as evident from the inset of the **Figure 7a** following equation described earlier [77-79]. In presence of rGO, the peak for formation of PtOH for different samples of Pt/rGO composites arises at more negative potential indicating rGO surface is more easily oxidized due to presence of several oxygen containing groups in rGO, plausibly following the quasi-reversible reaction:

$$rGO + OH^- \rightleftharpoons rGO - (OH)ads + e^-$$

The adsorption and release of OH^- ions by various functional groups of rGO make the nature of CV curve almost rectangular indicating well pseudo capacitive behavior of the electrodes. However, the current values are increased due to both faradic charge transfer and non faradic double layer capacitive effect. The current value in some cases [Pt/rGO-40, Pt/rGO-80]. are significantly high so that the second peak is not even visible The peak current values (presented in mA mg^{-1} within the parenthesis) of Pt-OH formation for the different electrodes follow the order: Pt/rGO-40 (34.26) > Pt/rGO-80 (20.38) > Pt/rGO-60 (19.75) > Pt/rGO-28 (4.52) > Pure Pt (1.19), indicating the beneficial role of rGO on the oxidation of the surface of composites which in turn helps methanol oxidation. The capacity current plays a definite role in all the carbon

based fuel cell catalysts but its contribution, particularly when current drawn is high, is yet not studied. Here the capacity current plays a significant role in presence of rGO, so its contribution is determined from the overall peak current i_p which can be expressed by

$$i_p = K_1 v^{1/2} + K_2 v$$

where, v is the scan rate and $K_1 v^{1/2}$ and $K_2 v$ are respectively contributions of redox charge transfer current and capacity current. So, a linear plot of $\frac{i_p}{v^{1/2}}$ versus $v^{1/2}$ (**Figure 7b**) is expected to provide constants K_1 and K_2 from the intercept and slope. Thus one can get the contributions of both the redox charge transfer current density ($K_1 v^{1/2}$) and non faradic capacity current density ($K_2 v$) at different conditions, i.e. when lower and higher currents are drawn. The values of K_1, K_2 and relative contributions of capacity and charge transfer current for Pt oxidation (hydroxyl adsorption) reaction at different scan rates are presented for different electrodes in **Table 4**. The data of the **Table 4** reveal that the capacity current arising from double layer charging-discharging is greater than the charge transfer current of metal oxidation, particularly at higher scan rate or when the current drawn is high. This result is consistent with highly reversible character of the double layer capacitors. At the scan rate of 0.02V s^{-1} the peak current contribution due to redox charge transfer is greater than peak current contribution due to double layer charging for Pt/rGO-40 and Pt/rGO-80 electrodes. Analysis of the 'current' data at the scan rates of 0.02 and 0.3 Vs^{-1} reveal that Pt/rGO-60 is the best electrode for squeezing non faradic capacity current among the different electrodes, whereas Pt/rGO-40 is the best for overall and Pt oxidation current density. Thus overall surface oxidation with the formation of rGO-(OH)ads and Pt-OH bonds occurs more extensively on the surface of Pt/rGO-40 than that on other electrodes.

20

Figure 7c depicts the CV profiles of MOR on the different electrodes studied. The characteristic CV data are presented in **Table 5**. It shows that Pt/rGO-28 and Pt/rGO-40 electrodes have higher values of forward peak potential (E_f) than pure Pt, pure rGO and all other Pt/rGO electrodes, indicating more oxidation of carbonaceous species effectively in the process of complete oxidation of methanol for these electrodes. The greater capability of these two electrodes towards complete oxidation of methanol might be due to the greater presence of Pt_3O_4 and facile oxidation of Pt to Pt-OH for Pt/rGO-40 electrode. The forward peak current density (I_f) of Pt/rGO composites are found to be comparable with the literature data presented in **Table S1** of the supporting document. The I_f values obtained by us is greater than these obtained in several studies [45, 48, 53] plausibly because of the fact that our catalyst possesses optimum defect sites containing oxygen. Some other studies [54, 56] also show greater current density than that of ours because of various reasons like smaller size, preferable geometrical shapes, etc. In this study, I_f of Pt/rGO-40 electrode is greater by 7.7 and 65.4 times than these for pure Pt and pure rGO electrodes. All the Pt/rGO electrodes exhibit greater peak current densities than that of pure Pt and rGO for MOR. This reveals the enhanced and synergistic electrocatalytic effect of the composites of Pt with rGO. Since overall specific peak current (mA mg^{-1} of Pt) has generated from the contributions of both the pseudo capacitance of Pt/rGO and the charge transfer due to MOR on the corresponding electrode, the respective residual current values of pseudo capacitance constituting non-Faradic double layer charging and Faradic charge transfer for oxidation of metal on the surface are subtracted from the overall forward and backward peak current values (I_f and (I_b) to get the current density solely from MOR (I'_f and I'_b). The computation of I'_f due to MOR is shown here at the inset of **Figure 7c** by drawing a straight line from the onset potential up to the peak potential and computing the current difference of the peak

and this straight line at the peak potential. The component of forward peak current density for MOR (I'_f) of Pt/rGO-40 is increased by 5.6 and 287 times than these for pure Pt and rGO electrodes respectively. I_f/I_b or I'_f/I'_b ratios which are advocated as poison tolerance capability of the electrodes are much higher than these of some literature available works of MOR in acid media [45, 48]. In spite of greater functionalities (Raman effect, capacity current) of Pt/rGO-60 and Pt/rGO-80, these electrodes exhibit weaker catalytic activity than Pt/rGO-40, plausibly because that the greater formation of rGO-(OH)ads on the surface may lead to reduction of free Pt sites due to formation of more than sufficient Pt-OH by spill over of the hydroxyl group following reaction

$$Pt + rGO\text{-}(OH)ads = Pt\text{-}OH + rGO$$

On increasing the temperature of the synthesis, the number of sp^2 C-OH increases at the rGO surface, as evident from FTIR studies of the as synthesized Pt-rGO composites. The surface bound -OH groups (S-OH) which contains both surface rGO-$(OH)_{ads}$ and Pt-OH may help in removal of Pt-CO by the reaction [80]

$$\textbf{Pt-CO + S-OH = Pt + S + CO}_2 \textbf{ + H}^+ \textbf{ + e}^-$$

At the higher temperature of synthesis, the number of epoxy groups per rGO sheet may be increased due to better reduction of –COOH, -CH_2OH and C=O groups present in GO, thus the poison removal capacity of rGO synthesized at higher temperature increases. **Figure 8** displays plausible mechanism of methanol oxidation on rGO surface in presence of Pt. The figure illustrates the formation and utilization of surface –OH (sp^2 C-OH) in oxidation of dissociative fractions of methanol like Pt-CH_2OH and Pt-CO to produce CO_2.

22

3.3.2. Tafel study

Based on Butler-Volmer equation, the apparent exchange current densities (i_0) for MOR on different electrodes have been estimated according to the relation:

$$E_{obs} = (a + Ee) + b\, logi, \text{ where, over potential,}$$

$$\eta = (E - Ee) \text{ and, } a = -b\log i_0$$

From the linear plot of E_{obs} versus $logi$ (**Figure 9a**) would give $(a + Ee)$ as the intercept and 'b' as the Tafel slope. Notably, $b = \dfrac{2.303RT}{\alpha F}$ where, R, T, α and F are the gas constant, absolute temperature, transmission coefficient and Faraday's constant respectively. The equilibrium potential, E_e is taken as (-0.9566 V) considering the oxidation of methanol to carbonate in 1 M alkali [62]. The calculated i_0 values are listed in **Table 6** which follows the sequences of Pt/rGO-40 > Pt/rGO-60 > Pt/rGO-80 > Pt/rGO-28. The data obtained from **Table 6** also revealed that the sequences of exchange current density followed the same order as obtained from potentio-dynamic polarization technique and the i_0 value of the best catalyst Pt/rGO-40 is 10^{27} times greater than that of Pt/rGO-28. Greater tafel slope indicates lower transmission co-efficient. Thus the transmission capability for oxidation of fuel increases in the order: Pt/rGO-40 < Pt/rGO-60 < Pt/rGO-80 < Pt/rGO-28. For Pt/rGO-28, reduction of Pt sites due to formation of Pt_3O_4 as evidenced from X-ray diffraction study, causes less methanol adsorption and hence less transmission co-efficient. For the first three electrodes transmission capability increases with the increase of temperature of the synthesis of catalyst because sp^2 C-OH increases in this order, which make the catalyst surface suitable for performing oxidation reaction.

3.3.3. Chronoamperometric investigations

The chronoamperometric technique was carried out to compare the constant potential behavior of different catalysts in the solution of 0.5M MeOH in 1M NaOH at -0.2 V, a potential very near to the peak potential of methanol oxidation in alkali media (**Figure 9b**). The decay in current in all the catalysts arises due to the gradual accumulation of poisoning species generated from methanol oxidation at electrode-electrolyte interface as well as the associated formation of Pt-oxides [81] which reduce the free sites of Pt on the surface for necessary methanol adsorption. The initial and limiting current for Pt/rGO-40 is higher than other catalysts throughout the entire range of 600 s indicating strong intermediate species tolerance and enhanced methanol oxidation activity. The order of current density is in accordance with that derived from CV study. At the end of 600s, the current density on Pt/rGO-40 electrode is still nearly 15 times higher than that on Pt/rGO-28 electrode. These findings conclude that Pt/rGO-40 catalyst exhibits the best electrocatalytic activity among the electrodes studied for methanol electro oxidation. **Figure 9c** illustrates that the peak current of CV and steady current of CA increase with decrease of I_D/I_G ratio for different catalysts. This indicates that lesser the defect sites, greater is the overall electrocatalytic activity plausible due to increase of the charge transfer (conductance) characteristic of the catalysts. Notably, the number of defect sites is minimal for Pt/rGO-40 catalyst. For Pt/rGO-28, formation of multilayer and Pt_3O_4 cause charge transfer (electron hoping) difficult whereas better exfoliation is responsible for lower charge transfer for electrodes like Pt/rGO-60 and Pt/rGO-80.

3.3.4. Stability of catalysts

To evaluate the long term stability of the catalysts, multi scan CV experiment has been performed with Pt/C and Pt/rGO-40 catalysts, by applying 500 consecutive triangular sweeps of

potential. The profiles of the mass normalized current versus cycle number of the multi scan experiment are shown in **Figure 10**. It is found that peak current density initially decreases very sharply plausibly due to loss of some Pt containing GO layer due to lack of well adherence of GO with the graphite substrate. But after about 100 cycles it attends a steady value indicating no further loss of Pt containing GO layer from the surface. This peak current density of Pt/rGO-40 of the 100th cycle is about 84.84 mA/mg of Pt while the value of pure Pt electrode at this cycle is ca 16.94 mA/mg of Pt. It is found that about 88.6% of the forward peak current density of the 100th cycle retains at the 500th cycle for Pt/rGO-40, but only 43% for Pt/C. It is also noted that, the current density on Pt/rGO-40 is much higher than those on Pt/C catalyst. These confirmed that Pt/rGO-40 catalyst exhibits greater cycling stability compared with Pt/C catalyst.

3.3.5. Electrochemical Impedance Study (EIS)

Nyquist profiles obtained from the EIS study at -0.1 V, shows initial semicircular trend at higher frequency and upward rising trend at lower frequency, as expected. The higher frequency region provides the signature of the fast processes i.e. that occur at the surface, whereas the lower one which involves much time provides the characteristics of the inner layer. Accordingly, the impedance data for all the electrodes fit well with an equivalent circuit (inset of **Figure 11**) consisting of solution resistance and two loops in series. Each loop contains a capacitor and a resistor in parallel. The solution resistance R_S varies between the lowest values of 0.6588 Ω for pure Pt to the highest value of 0.78336 Ὠ for the sample Pt/rGO-40 (**Table 7**), indicating insignificant practical change of solution resistance, as the electrolyte is same for all the electrodes. The highest value of R_S for Pt/rGO-40 might be due to maximum accumulation of the products at the surface. The first closed loop after R_s consists of charge transfer resistance due to catalytic reaction of MOR on Pt nanoparticles at the surface and the capacitor due to

25

accumulation and release of surface-intermediates and ions, in parallel with each other. The second closed loop also contains the same type of resistor and capacitor elements but pertained with the interiors of the materials. The component of phase element at constant time (CPE-T) is found to be very small for Pt and rGO and the greatest for Pt/rGO-40. Again when phase is constant, the phase element (CPE1-P) is found to be nearly 1 for rGO, pure Pt and Pt/rGO-80 whereas it is nearly 0.5 for Pt/rGO-40. This indicates that non faradic charge transfer process dominates for the former group of electrodes, while faradic charge transfer process dominates for Pt/rGO-40. The values of CPE1-P (n) being intermediate between 0.5 and 1, it indicates that both faradic and non-faradic charge transfer processes are contributing significantly in the overall electrochemical process. The charge transfer resistance among the binary composites at the surface (R_{Ct1}) varies in the order: Pt/rGO-40 > Pt/rGO-60 > Pt/rGO-28 > Pt/rGO-80. This is plausibly due to the fact that when the effective diameter of the nanoparticle is greater, it is less bound by the hydration or the capping layer of the electrolyte, thus the reaction molecule can approach to the active Pt-sites without any hindrance. The closed loop 2 consisting of a capacitor and resistor in parallel, illustrates the charge transfer process occurring at the inner layer of rGO. Here both the constant phase elements CPE2-T and CPE2-P are greater in respect to the corresponding elements of loop 1, due to hindrance faced by the ions and reactant molecules inside the inner layers of rGO. The corresponding charge transfer resistance R_{Ct2} is also high in respect to that occurring at the outer surface. The R_{Ct2} values change in the order: Pt/rGO-40 < Pt < Pt/rGO-60 < Pt/rGO-80 < Pt/rGO-28 ≈ rGO, indicating that Pt/rGO-40 is the best catalyst material in absence of significant hydrating / capping layer inside the rGO layers. Since the overall charge transfer must proceed through the inner surface, the overall resistance/impedance

is guided by the second loop and the least impedance is found for the Pt/rGO-40 among the different electrodes studied.

The greater anodic activity of Pt/rGO-40 is seemingly due to optimum presence of free surface sites of Pt for initial methanol adsorption and rGO-(OH)$_{ads}$ on the surface for its oxidation. The lower anodic activity of Pt/rGO-28 is due to lower Pt surface for methanol adsorption for conversion of some Pt sites to Pt$_3$O$_4$ as found in the XRD study. On the other hand, lower activity for Pt/rGO-60 and Pt/rGO-80 electrodes in comparison to that for Pt/rGO-40, might be due to the significant coverage of surface-sites by formation of S-OH which includes both rGO-(OH)ads and Pt-OH and thus methanol adsorption is disturbed and hence anode catalytic activity is decreased. Further to add, increase in interlayer rGO separation with increase of synthesis temperature as explained in Raman study, enhances the interfacial charge transfer resistance that causes elevation of overall Rct$_2$ value for these systems.

4. Conclusion

We report facile temperature control synthesis of Pt nanoparticles of varying diameter decorated on rGO surface containing different extent of oxygen functionalities for use of these as anode catalyst materials for oxidation of methanol in alkali. The catalysts synthesized at various temperatures are successfully characterized by XRD, TEM, FESEM, TGA, XPS studies and found to exhibit improved and synergistic catalytic activity in comparison to pure Pt and rGO in reference to MOR in alkali. The overall current values are contributed by charge transfers of both pseudo capacitance of Pt decorated rGO and MOR in alkali. The poison tolerance parameter based on the ratio of forward and backward charge transfer contributions of peak currents for MOR, I'$_f$/I'$_b$ is higher in comparison to data found in the literature for Pt/rGO composites and also mostly increases for the catalysts synthesized at higher temperature. The composites synthesized

at higher temperature exhibit high optical density ratio for the peaks of sp^2 C-OH and that of C-O-C(epoxy) as obtained from FTIR and defect parameter as measured by I_D/I_G in Raman study, indicating a direct co-relation between poison tolerance and defect sites. However, the best catalytic activity among the Pt/rGO composites was obtained from the catalyst synthesized at an optimum temperature of 40ºC. For this catalyst, adsorption of hydroxyl group is the greatest as evidenced from the cycle voltammetric study in sole alkali indicating less spill over of –OH group from rGO to the metal surface causing more availability of Pt sites for adsorption of both –OH group and methanol. Formation of greater Pt_3O_4 in Pt/rGO material synthesized at 28°C also causes for less methanol adsorption and relatively slow kinetics in comparison to that at 40^0C temperature. The presence of greater Pt metallic surface surrounded by lower but sufficient oxygen functionalities arising from mainly sp^2 C-OH on rGO support as evidenced by FTIR and Raman studies seems to be important for further improvement in catalysis.

ACKNOWLEDGEMENTS

REFERENCES

[1] A. Kirubakaran, S. Jain, R.K. Nema, *Renew Sust. Energ. Rev.* **2009**, *13*, 2430-2440.

[2] C. Lamy, A. Lima, V. LeRhun, F. Delime, C. Coutanceau, J.M. Léger, *J. Power Sources*, **2002,** *105,* 283-296.

[3] A. Mehmood, M.A. Scibioh, J. Prabhuram, M.G. An, H.Y. Ha, *J. Power Sources,* **2015,** *297*, 224-241.

[4] P. Joghee, J.N. Malik, S. Pylypenko, R.O. Hayre, *MRS Energy Sustain. Rev. J.* **2015,** *2,* 1-31.

[5] V. Baglio, A.D. Blasi, E. Modica, P. Cretì, V. Antonucci, A.S. Aricò, *Int. J. Electrochem. Sci.* **2006**, *1*, 71-79.

[6] R.N. Singh, R. Awasthi, C.S. Sharma, *Int. J. Electrochem. Sci.* **2014**, *9*, 5607-5639.

[7] G. Sevjidsuren, S. Zils, S. Kaserer, et al., *Journal of Nanomaterials*, Article ID 852786, **2010**, 9 pages,.

[8] S. Cao, F. Tao, Y. Tang, Y. Li, J. Yu, *Chem. Soc. Rev.* **2016**, *45*, 4747-4765.

[9] J. Wang, H. Gu, *Molecules*, **2015**, *20*, 17070-17092.

[10] C. Wang, H. Daimon, T. Onodera, T. Koda, S.H. Sun, *Angew. Chem.* **2008**, *120*, 3644-3647.

[11] P.S. Roy, J. Bagchi, S.K. Bhattacharya**,** *Transition Met Chem.* **2009**, *34*, 447-453.

[12] P.S. Roy, S.K. Bhattacharya, *RSC Adv.* **2014**, *4*, 13892-13900.

[13] Y. Shen, K.J. Xiao, J.Y. Xi, X.P. Qiu, *J. Power Sources*, **2015**, *278*, 235-244.

[14] P. Song, L.L. He, A.J. Wang, L.P. Mei, S.X. Zhong, J.R. Chen, J.J. Feng, *J. Mater. Chem. A*, **2015**, *3*, 5321-5327.

[15] D. Villers, S.H. Sun, A.M. Serventi, J.P. Dodelet, *J. Phys. Chem. B*, **2006**, *110*, 25916-25925.

[16] C. Gupta, P.H. Maheshwari, S.R. Dhakate, *Mater Renew Sustain Energy*, **2016,** 5:2.

[17] X.X. Wang, Z.H. Tan, M. Zeng, J.N. Wang, *Sci Rep.* **2014**, *4*, article number: 4437.

[18] D. Prasanna, V. Selvaraj, Korean *J. Chem. Eng.* **2016**, *33*, 1489-99.

[19] C.C. Hung, P.Y. Lim, J.R. Chen, H.C. Shih, *J. Power Sources*, **2011**, *196*, 140-146.

[20] K. Miyazaki, H. Shirakata, T. Abe, N. Yoshizawa, Z. Ogumi, *Fuel Cells*, **2010**, *10*, 960-965.

[21] X. Tong, H. Wang, G. Wang, L. Wan, Z. Ren, J. Bai, J. Bai, *J. Solid State Chem*., **2011**, *184*, 982-989.

[22] Q. Zhuo, Y. Ma, J. Gao, P. Zhang, Y. Xia, Y. Tian, X. Sun, J. Zhong, X. Sun, *Inorg. Chem*., **2013**, *52*, 3141-3147.

[23] L. Zheng, D. Ye, L. Xiong, J. Xu, K. Tao, Z. Zou, D. Huang, X. Kang, S. Yang, J. Xia, *Analytica Chimica Acta,* **2013,** *768*, 69-75.

[24] A. Mahajan, S. Banik, D. Majumdar, S.K. Bhattacharya, *ACS Omega,* **2019,** *4 (3),* 4658-4670.

[25] A.K. Geim, K.S. Novoselov, *Nat Mater.* **2007**, *6*, 183-191.

[26] M.J. Allen, V.C. Tung, R.B. Kaner, *Chem. Rev.* **2010**, *110*, 132-145.

[27] E.P. Randviir, D.A.C. Brownsonm, C. E. Banks, *Mater Today*, **2014**, *17*, 426-432.

[28] M.L. Yola, N. Atar, T. Eren, H.K. Maleh, S. Wang, *RSC Advances*, **2015**, *5*, 65953-65962

[29] N. Atar, T. Eren, M.L. Yola, H. Gerengi, S. Wang, *Ionics*, **2015**, *21*, 3185-3192.

[30] N. Atar, T. Erena, M.L. Yola, *Thin Solid Film*, **2015,** *590*, 156-162.

[31] S. Elcin, M.L. Yola, T. Eren, B. Girgin, N. Atar, *Electroanalysis*, **2016,** *28*, 611-619.

[32] G. Kotan, F. Kardas, O.A. Yokus, O. Akyıldırım, H. Saral, T. Eren, M.L Yola, N. Atar, *Analytical Methods*, **2016,** *8*, 401-408.

[33] Ö.A. Yokus, F. Kardas, O. Akyıldırımc, T. Erend, N. Atard, M.L. Yolae, *Sensors and Actuators B: Chemical*, **2016,** *233,* 47-54.

[34] O. Akyıldırım, H. Yuksek, H. Saral, I. Ermis, T. Eren, M.L Yola, *Journal of Materials Science*: *Materials in Electronics*, **2016**, *27*, 8559-8566.

[35] T. Kuila, S. Bose., A.K Mishra, P. Khanra, N.H. Kim, J.H. Lee., *Progress in Materials Science*, **2012**, *57,* 1061-1105.

[36] C. Berger, Z. Song, T. Li, X. Li, A.Y. Ogbazghi, R. Feng, Z. Dai, A.N. Marchenkov, E.H. Conrad, P.N. First., W.A. de Heer, *J. Phys. Chem. B*, **2004**, *108*, 19912-19916.

[37] E. Lacatus, *Materials Today: Proceedings,* **2016**, *8*, 2635-2645.

[38] S. Alwarappan, S. Boyapalle, A. Kumar, C.Z. Li, S Mohapatra, *J. Phys. Chem. C*, **2012,** *116*, 6556-6559.

[39] Y. Xin, J.G. Liu, Y. Zhou, W. Liu, J. Gao, Y. Xie, Y. Yin, Z. Zou, *J. Power Sources*, **2011**, *196*, 1012-1018.

[40] S. Marzena, J.Z. Wietecha, G. Guihua, W. Ning, F. Huan, L.G. Matthew, L. Marc, S.H. Kasner, *J. Power Sources*, **2012**, *198*, 30-35.

[41] D. Inhwan, T.D. Lawrence, *ACS Appl. Mater. Interfaces*, **2014**, *6*, 12126-12136.

[42] G.K. Georgepeter, J.K. Christopher, U.K. Subramani, K. Chandrasekaran, S.N. Kee, *Ind. Eng. Chem. Res.* **2014**, *53*, 16883-16893.

[43] Y. Li, L. Tang, J. Li, *Electrochem. Comm.* **2009**, *11*, 846-849.

[44] S. Wu, J. Liu, Z. Tian, Y. Cai, Y. Ye, Q. Yuan, C. Liang, *ACS Appl. Mater. Interfaces*, **2015**, *7*, 22935-22940.

[45] X. Zhang, N. Hao, X. Dong, S. Chen, Z. Zhou, Y. Zhang, K. Wang, *RSC Adv.* **2016**, *6*, 69973-69976.

[46] T. Radhakrishnan, N. Sandhyarani, *Int. J. Hydrogen Energy*, **2017**, *42*, 7014 -7022.

[47] L. Zhao, X.L. Sui, J.L. Li, J.J. Zhang, L.M. Zhang, Z.B. Wang, *ACS Appl. Mater. Interfaces*, **2016**, *8*, 16026-16034.

[48] H. Huang, G. Ye, S. Yang, H. Fei, C.S. Tiwary, Y. Gong, R. Vajtai, J. M. Tour, X. Wang P.M. Ajayan, *J. Mater. Chem. A*, **2015**, *3*, 19696-19701.

[49] X. Xu, Y. Zhou, T. Yuan, Y. Li, *Electrochim. Acta*, **2013**, *112*, 587-595.

[50] B. Xiong, Y. Zhou, Y. Zhao, J. Wang, X. Chen, R. Hayre, Z. Shao, *Carbon*, **2013**, *52*, 181-192.

[51] B. Luoa, X. Yana, S. Xuc, Q. Xuea, *Electrochim. Acta*, **2012**, *59*, 429-434.

[52] Y. Xina, J.G. Liua, Y. Zhoua, W. Liua, J. Gao, Y. Xie, Y. Yinb, Z. Zoua, *J. Power Sources*, **2011**, *196*, 1012-1018.

[53] M.S. Wietecha, J. Zhu, G. Gao, N. Wang, H. Feng, M.L. Gorring, M.L. Kasner, S. Hou, *J. Power Sources*, **2012**, *198*, 30-35.

[54] K. Kakaei, M. Zhiani, *J. Power Sources*, **2013**, *225*, 356-363.

[55] Y.G. Zhou, J.J. Chen, F.B. Wang, Z.H. Sheng, X.H. Xia, *Chem. Commun.* **2010**, *46*, 5951-5953.

[56] L. Zhao, X.L. Sui, J.L. Li, J.J. Zhang, L.M. Zhang, Z.B. Wang, *J. Mater. Chem. A*, **2015**, *3*, 5313-5320.

[57] Y. Li, W. Gao, L. Ci, C. Wang, P.M. Ajayan, *Carbon*, **2010**, *48*, 1124-1130.

[58] J.D. Qiu, G.C. Wang, R.P. Liang, X.H. Xia, H.W. Yu, *J. Phys. Chem. C*, **2011**, *115*, 15639-15645.

[59] Y. Wang, J. Liu, L. Liu, D.D. Sun, *Nanoscale Res Lett*. **2011**, *6*, 241-249.

[60] D.Y. Chung, K.J. Lee, Y.E. Sung, *J. Phys. Chem. C*, **2016**, *120*, 9028-9035.

[61] S. Park, J. An, R.D. Piner, I. Jung, D. Yang, A. Velamakanni et al. *Chem Mater*. **2008**, *20*, 6592-6594.

[62] S. Banik, A. Mahajan, S.R. Chowdhury, S.K. Bhattacharya, *RSC Adv*. **2016**, *6*, 92490-92501.

[63] S. Wu, J. Liu, Z. Tian, Y. Cai, Y. Ye, Q. Yuan, C. Liang, *ACS Appl. Mater. Interfaces*, **2015**, *7*, 22935-22940.

[64] J.D. Qiu, G.C. Wang, R.P. Liang, X.H. Xia, H.W. Yu, *J. Phys. Chem. C*, **2011**, *115*, 15639-15645.

[65] A.K. Zak, W.H. Abd Majid, M.E. Abrishami, R. Yousefi, *Solid State Sciences*, **2011**, *13*, 251-256.

[66] Y.K. Lin, R.S. Chen, T.C. Chou, Y.H. Lee, Y.F. Chen, K.H. Chen, L.C. Chen, *ACS Appl. Mater. Interfaces*, **2016**, *8*, 22637-22646.

[67] Z. Li, W. Zhang, Y. Luo, J. Yang, J.G. Hou, *J. Am. Chem. Soc*. **2009**, *131*, 6320-6321.

[68] S.K. Saha, M. Baskey, D. Majumdar, *Adv. Mater*. **2010**, *22*, 5531-5536.

[69] A.C. Ferrari, *Solid State Communications*, **2007**, *143*, 47-57.

[70] D. Wei, Y. Liu, Y. Wang, H. Zhang, L. Huang, G. Yu, *Nano Lett*. **2009**, *9*, 1752-1758.

[71] G. Saravanana, S. Mohan, *Appl. Surf. Sci*. **2016**, *386*, 96-102.

[72] M.M. Lucchese, F. Stavale, E.H. Martins Ferreira, C. Vilani, M.V.O. Moutinho, R.B. Capaz, C.A. Achete, A. Jorio, *Carbon*, **2010**, *48*, 1592-1597.

[73] K. Krishnamoorthy,·M. Veerapandian,·R. Mohan,·S.J. Kim, *Appl Phys A*, **2012**, *106*, 501-506.

[74] V.T. Nguyen, H.D. Le, V.C. Nguyen, T.T.T. Ngo, D.Q. Le, X.N. Nguyen, N.M. Phan, *Adv. Nat. Sci.: Nanosci. Nanotechnol* **2013**, *4*, 035012 (5pp).

[75] B. Seger P.V. Kamat, *J. Phys. Chem. C*, **2009**, *113*, 7990-7995.

[76] S. Stankovich, D.A. Dikin, R.D. Piner, K.A. Kohlhaas, A. Kleinhammes, Y. Jia, Y. Wu, S.T. Nguyen, R.S. Ruoff, *Carbon*, **2007**, *45*, 1558-1565.

[77] P. Mukerjee, P.S. Roy, S.K. Bhattacharya, *Int. J. Hydrogen Energy*, **2015**, *40*, 1-11.

[78] P. Mukherjee, J. Bagchi, S. Dutta, S.K. Bhattacharya, *Appl Catal A*, **2015**, *506*, 220-227.

[79] J. Bagchi, S.K. Bhattacharya, *J Power sources*, **2007**, *163*, 661-670.

[80] S. Sharma, A. Ganguly, P. Papakonstantinou, X. Miao, M. Li, J.L. Hutchison, M. Delichatsios, S. Ukleja, *J. Phys. Chem. C*, **2010**, *114*, 19459-19466.

[81] S.R. Chowdhury, P. Mukherjee, S.K Bhattachrya, *Int. J. Hydrogen Energy*, **2016**, *41*, 17072-17083.

Figure Legends

Figure 1. PXRD patterns of: (a) graphite powder (black line) and graphene oxide (red line) (b) Synthesized Pt/rGO composites. The inset represents XRD patterns of Pt/ rGO-NPs with the 2θ between 15º and 35º

Figure 2. FESEM images of (a) rGO, (b) Pt/rGO-40 (low resolution ×30,000), (c) Pt/rGO-28, (d) Pt/rGO-40, (e) Pt/rGO-60, (f) Pt/rGO-80 (high resolution ×100,000) and the corresponding size distribution are presented in inset.

Figure 3. Representative TEM images of (a) Pt/rGO-40, (b) Pt nanoparticles without GO (c) HRTEM of Pt/rGO-40 (d) EDX pattern of Pt/rGO-40 sample.

Figure 4. XPS survey spectrum of Pt/rGO-40 (a), and core level spectra: (b) Pt 4f (c) O 1s (d) C 1s.

Figure 5. FTIR spectra of a) rGO, b) Pt/rGO-28, c) Pt/rGO-40, d) Pt/rGO-60, and e) Pt/rGO-80.

Figure 6. (a) Raman spectra of GO, Pt/rGO-28, Pt/rGO-40, and Pt/rGO-80, (b) Thermogravimetric analysis of graphene oxide and Pt doped graphene oxide. The lines (a, b) shows the change in weight while the lines (a', b') show the derivative of the change in weight with respect to temperature

Figure 7. (a) Cyclic voltammograms of the marked electrodes immersed in 1M NaOH at the scan rate of 50 mV/s (b) Plots of $i_p/v^{1/2}$ versus $v^{1/2}$ corresponding to the peak current, i_p of Pt-OH formation, "v" being the scan rate. The error limit presented has been computed on the basis of 5 different experiments of CV for each of the electrodes. (c) Cyclic voltammograms of MOR on all

37

the marked electrodes immersed in 0.5 M methanol in 1 M NaOH. The inset shows the method of computation of i'_f and i'_b for Pt/rGO-40 electrode.

Figure 8. Plausible mechanism of methanol oxidation reaction on rGO surface in presence of Pt.

Figure 9. (a) Tafel Polarization profiles (b) Chronoamperomatric profiles, of electrodes made of different Pt/rGO composites. (c) Plots of peak and steady current density versus parameter representing defect concentration. The inset shows the dependence of defect concentration with temperature.

Figure 10. Variation of Current Density with cycle number of Pt and Pt/rGO-40 sample has been shown for 500 cycles measured at scan rate 50 mV/s.

Figure 11. Nyquist plot of Pt, rGO and all the Pt/rGO composites electrodes recorded in 0.5 M methanol in 1 M NaOH solutions. Equivalent circuit is given at upper inset and magnified higher frequency region is given at lower inset.

Table 1 Size parameters and strain of differently synthesized supported catalysts.

Catalysts	Average radius of crystallites from Williamson-Hall method (nm)	Strain ($\times 10^{-3}$)	Average radius from FESEM (nm)
Pt/rGO-28	7.60	10.50	8.41
Pt/rGO-40	7.17	-5.60	7.41
Pt/rGO-60	6.26	0.189	14.85
Pt/rGO-80	4.16	-0.188	15.87

Table 2. Ratios of relative optical density of different stretching frequencies of FTIR bands of different catalysts.

Catalysts	$OD\frac{C-O-C}{C=C}$	$OD\frac{C-O-C}{C=O}$	$OD\frac{C=C}{C=O}$	$OD\frac{sp^2C-OH}{C-O-C}$
GO	1.602	1.844	1.151	0.7846
Pt/rGO-28	1.0675	1.128	1.0492	0.8894
Pt/rGO-40	0.9862	1.067	1.0735	0.8922
Pt/rGO-60	0.9604	1.006	1.0443	0.9230
Pt/rGO-80	0.9483	0.9794	1.0179	0.9984

Table 3: Data obtained from Raman spectroscopy

Catalysts	I_D	(D) cm^{-1}	I_G	(G) cm^{-1}	I_D/I_G	I_{2D}	(2D) cm^{-1}	I_{2D}/I_G ratio
GO	279.51	1355	279.26	1594	1.001	-	-	--
Pt/rGO-28	292.64	1350	251.40	1575	1.164	102.12	2667	0.4063
Pt/rGO-40	238.20	1348	211.30	1575	1.127	95.832	2694	0.4537
Pt/rGO-80	233	1347	202	1587	1.159	113.72	2686	0.5631

Table 4. Slopes and intercepts of $i_p/v^{1/2}$ versus $v^{1/2}$ plot and the contribution of capacity and metal oxidation charge transfer current and their ratio at the different scan rates : 0.02 and 0.3 (within parenthesis) V s^{-1}

Catalysts	Intercept (K_1) mA mg^{-1} V$^{-1/2}$	Slope (K_2) mA mg^{-1} V^{-1}	I_p(C) mA mg^{-1} of Pt	I_p(CT) mA mg^{-1} of Pt	$\dfrac{Ip(CT)}{Ip(C)}$
			Relative contribution of Capacity (C) & Charge Transfer (CT) current		
Pt/rGO-28	0.332	0.09	1.80 (27)	1.48 (5.75)	0.83 (0.21)
Pt/rGO-40	1.99	0.181	3.62 (54.3)	8.90 (34.46)	2.45 (0.63)
Pt/rGO-60	0.35	0.199	3.98 (59.7)	1.56 (6.062)	0.39 (0.1)
Pt/rGO-80	0.58	0.124	2.48 (37.2)	2.59 (10.04)	1 (0.27)

40

Table 5 Various electrocatalytic properties of synthesized Pt/rGO composites for the MOR, obtained from cyclic voltammetric studies at a scan rate of 50 mV s^{-1}

Catalysts	Onset Potential (V)	Loading of Pt (mg/cm^2)	E_f (V)	E_b (V)	Overall forward peak current density I_f (mA mg^{-1} of Pt)	Overall backward peak current density I_b (mA mg^{-1} of Pt)	Charge transfer forward peak current density $I_f^{'}$ (mA mg^{-1} of Pt)	Charge transfer backward peak current density $I_b^{'}$(mA mg^{-1} of Pt)	$I_f^{'}/I_b^{'}$
Pt	-0.502	1.38	-0.158	-0.29	15.22	4.06	11.72	5.47	2.14
Pt/rGO-28	-0.405	0.116	-0.045	-0.31	16.45	-10.58	6.33	3.19	1.98
Pt/rGO-40	-0.428	0.125	-0.05	-0.33	116.48	-13.11	66.06	14.21	4.67
Pt/rGO-60	-0.394	0.122	-0.08	-0.37	44.77	-20.11	15.67	2.03	7.71
Pt/rGO-80	-0.406	0.125	-0.1	-0.35	29.96	-17.71	9.92		
rGO	-0.42		-0.2		1.78		0.23		

Table 6 Data from chronoamperometric and cyclic voltammetric studies

Catalysts	Steady current Density (mA mg^{-1} of Pt) obtained at (-0.2 V) in chronoamperometry	Apparent Tafel Slope (V dec^{-1}) (Scan rate 1mV s^{-1})	Apparent Exchange Current density, i_0 (mA mg^{-1})
Pt/rGO-28	0.92	0.028	4×10^{-30}
Pt/rGO-40	11.12	0.195	4.5×10^{-3}
Pt/rGO-60	2.7	0.082	8.5×10^{-9}
Pt/rGO-80	1.74	0.064	2.5×10^{-12}

Table 7 Various charge transfer parameters obtained from electrochemical impedance data using equivalent circuit model.

Catalysts	Series resistance (R_s) in Ω	CPE1		Charge transfer resistance (Rct_1) in Ω	CPE2		Charge transfer resistance (Rct_2) in Ω
		CPE1-T (F/cm^2)	CPE1-P (n)		CPE2-T (F/cm^2)	CPE2-P (n)	
Pt/rGO-28	0.67999	0.0007889	0.7655	0.61881	0.0078366	0.83168	8000
Pt/rGO-40	0.78336	0.012869	0.4966	1.7	0.024147	0.69	500
Pt/rGO-60	0.66252	0.00040547	0.6151	1.192	0.0081682	0.8	1000
Pt/rGO-80	0.76279	0.0000175	1.103	0.26758	0.0068446	0.668	2000
rGO	0.7687	0.000122254	1.01	0.31919	0.0049747	0.73727	8000
Pt	0.6588	0.00004826	0.9925	0.35053	0.002506	0.725	600

Figures

Figure 1
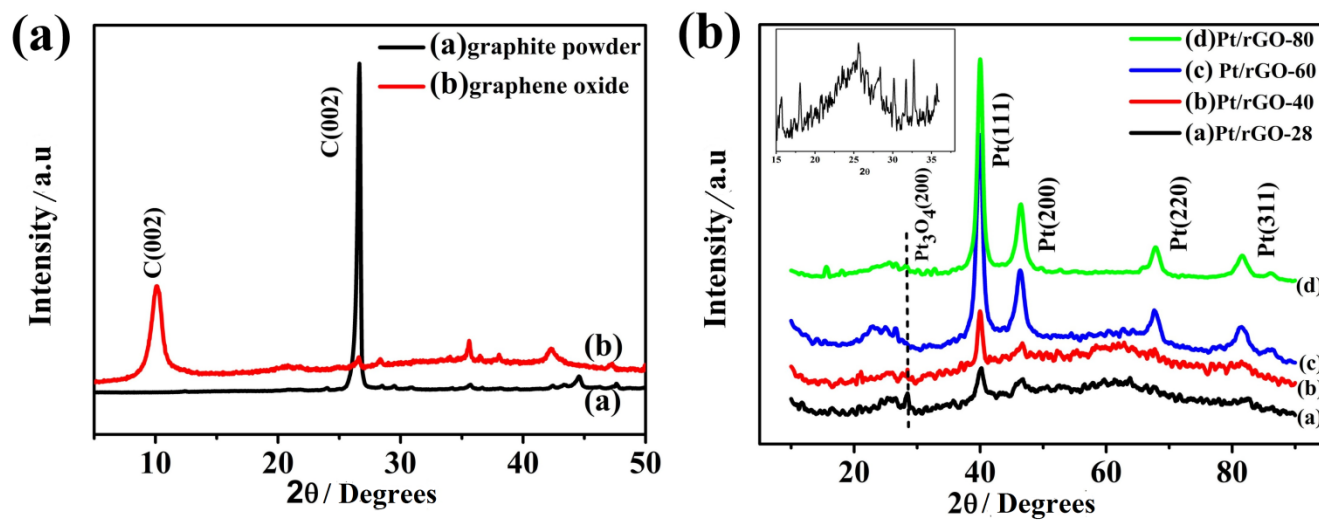
Figure 2
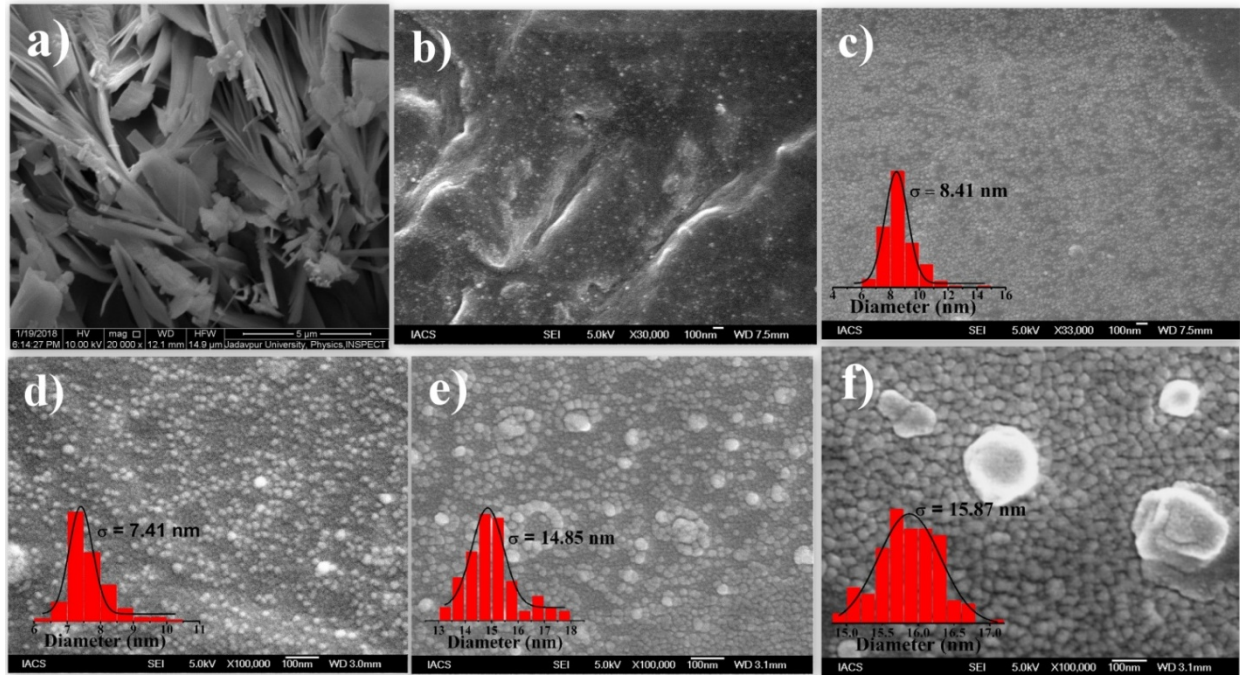
Figure 3
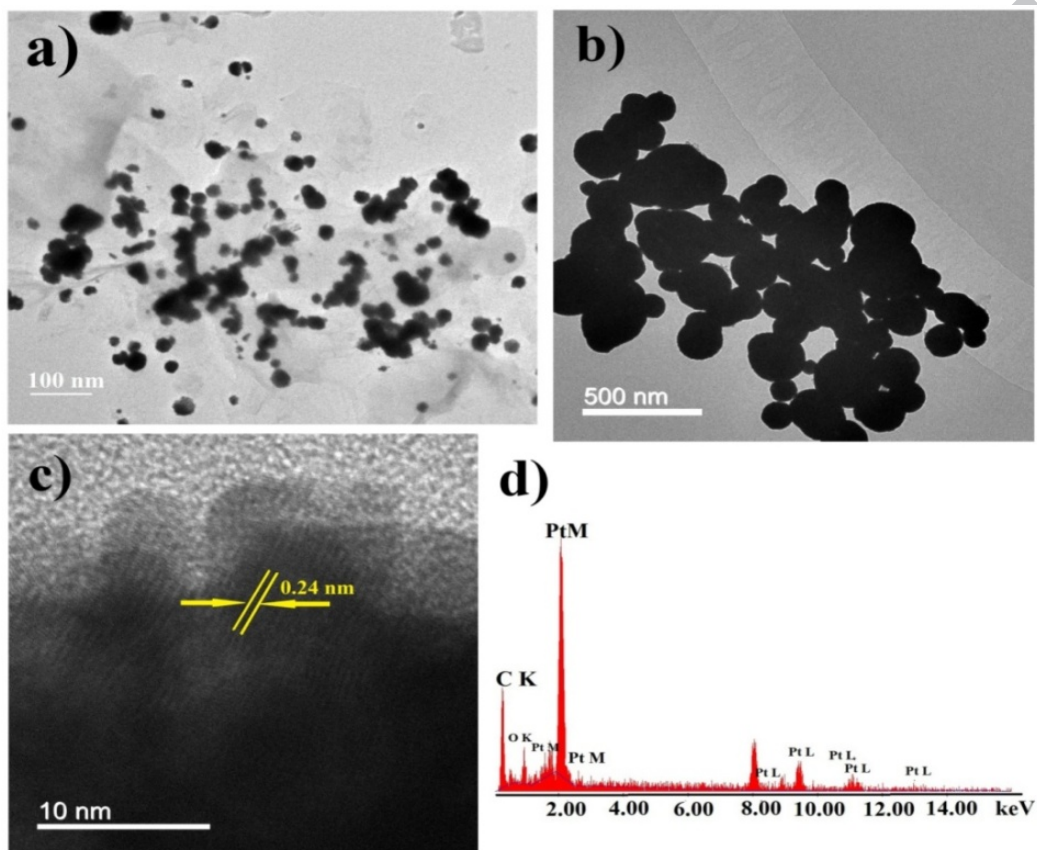
Figure 4
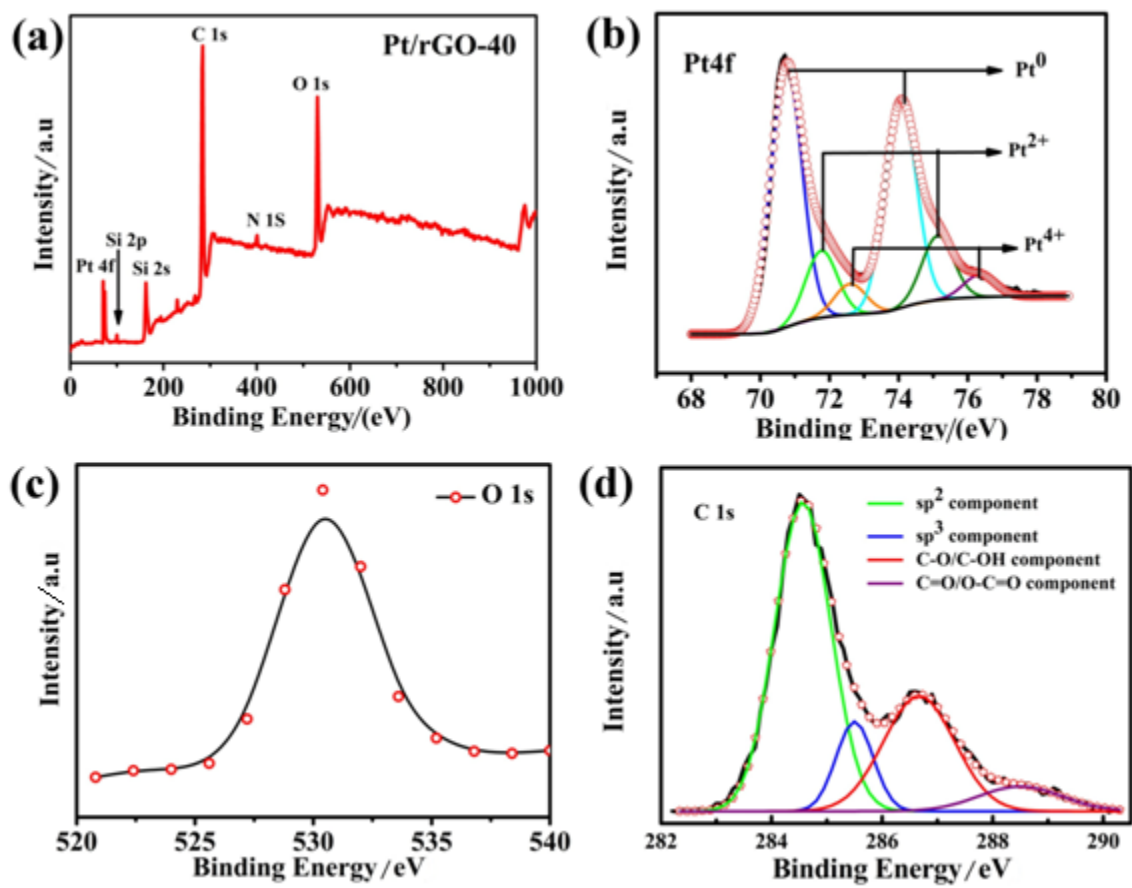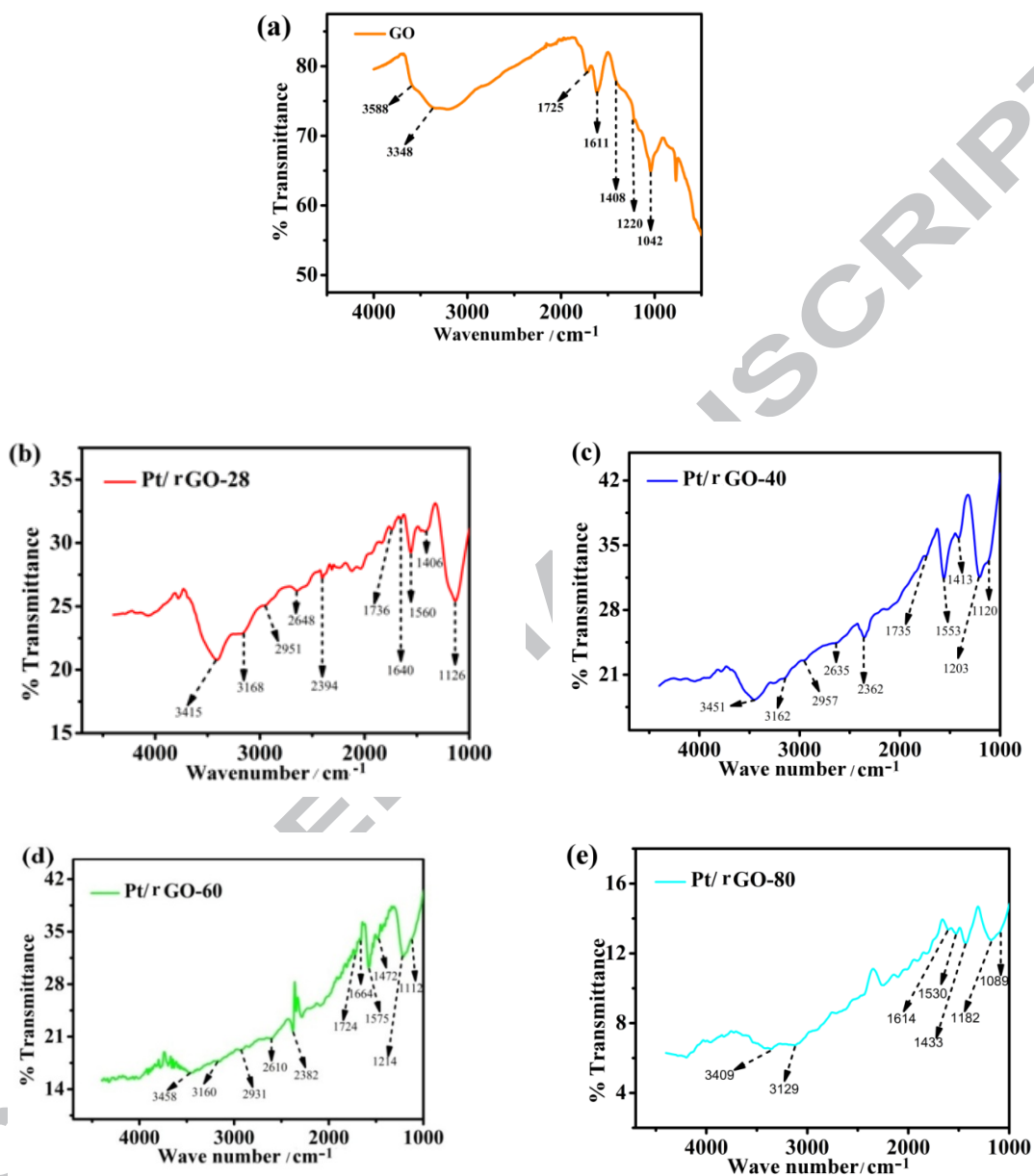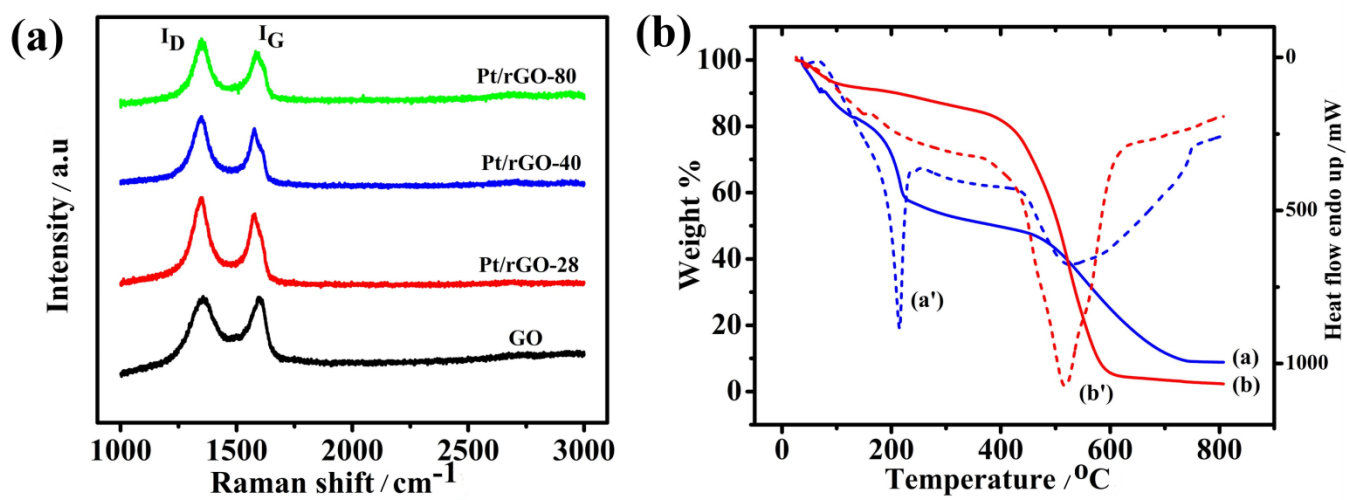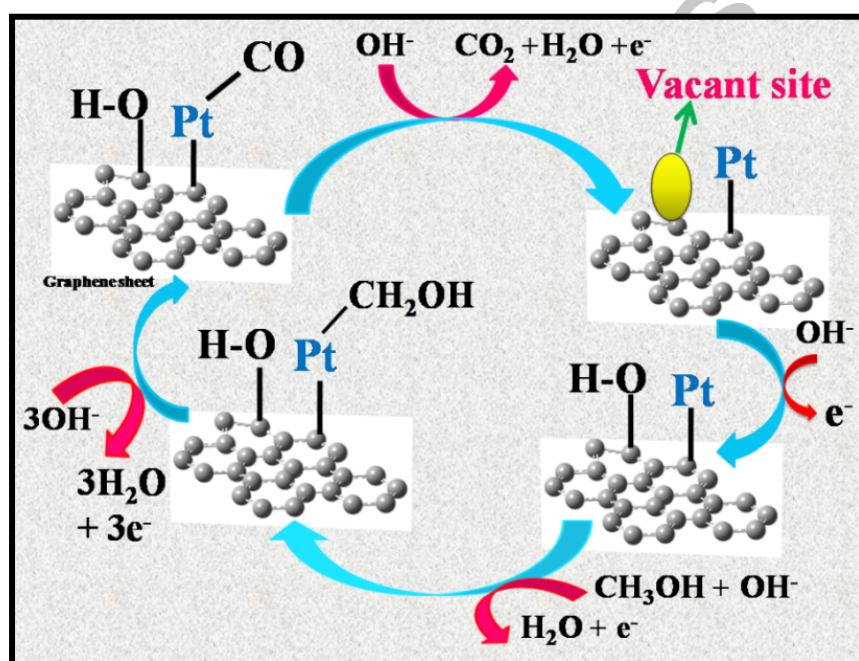
Figure 5

Figure 6

Figure 7
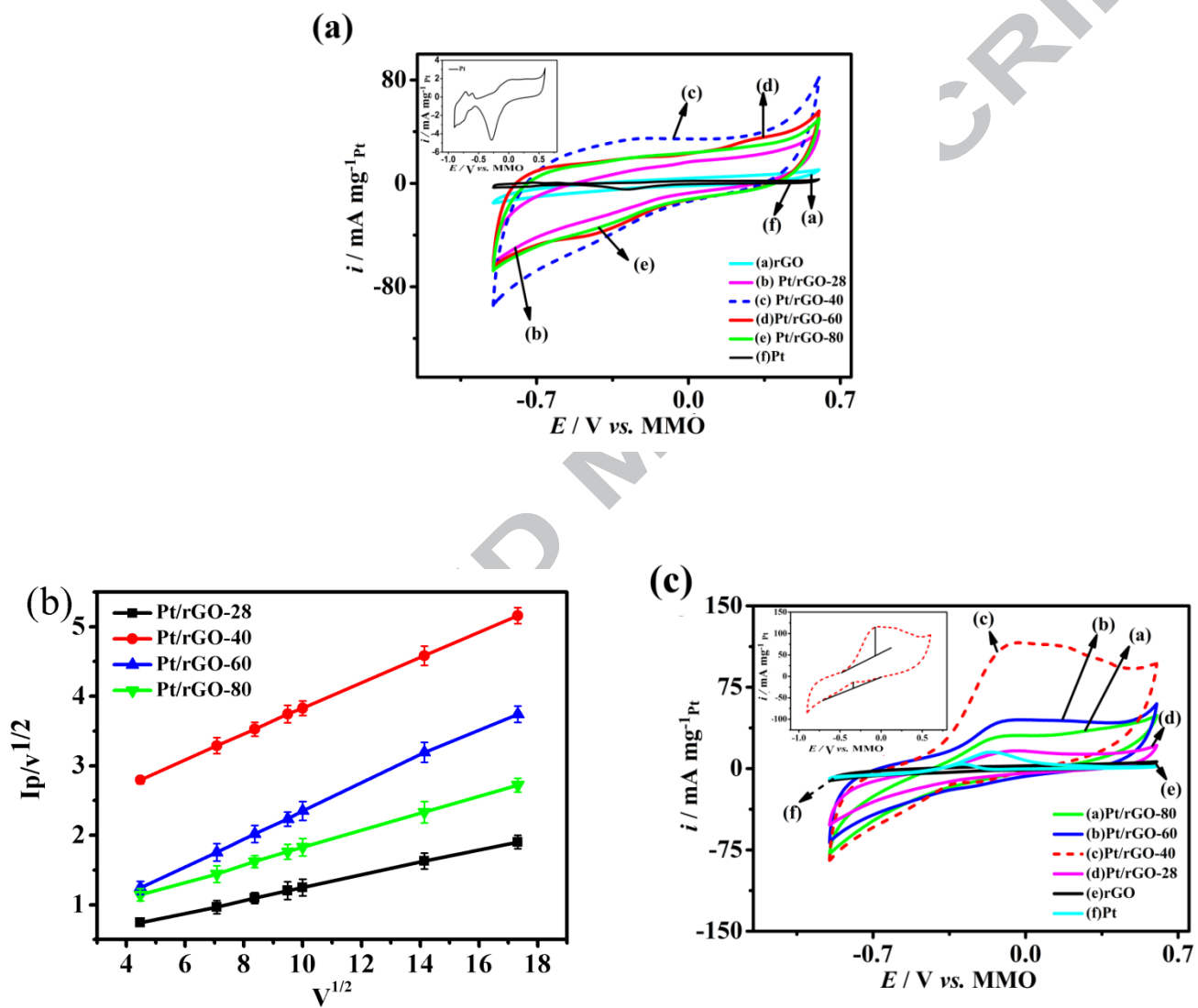
Figure 8

Figure 9

Figure 10

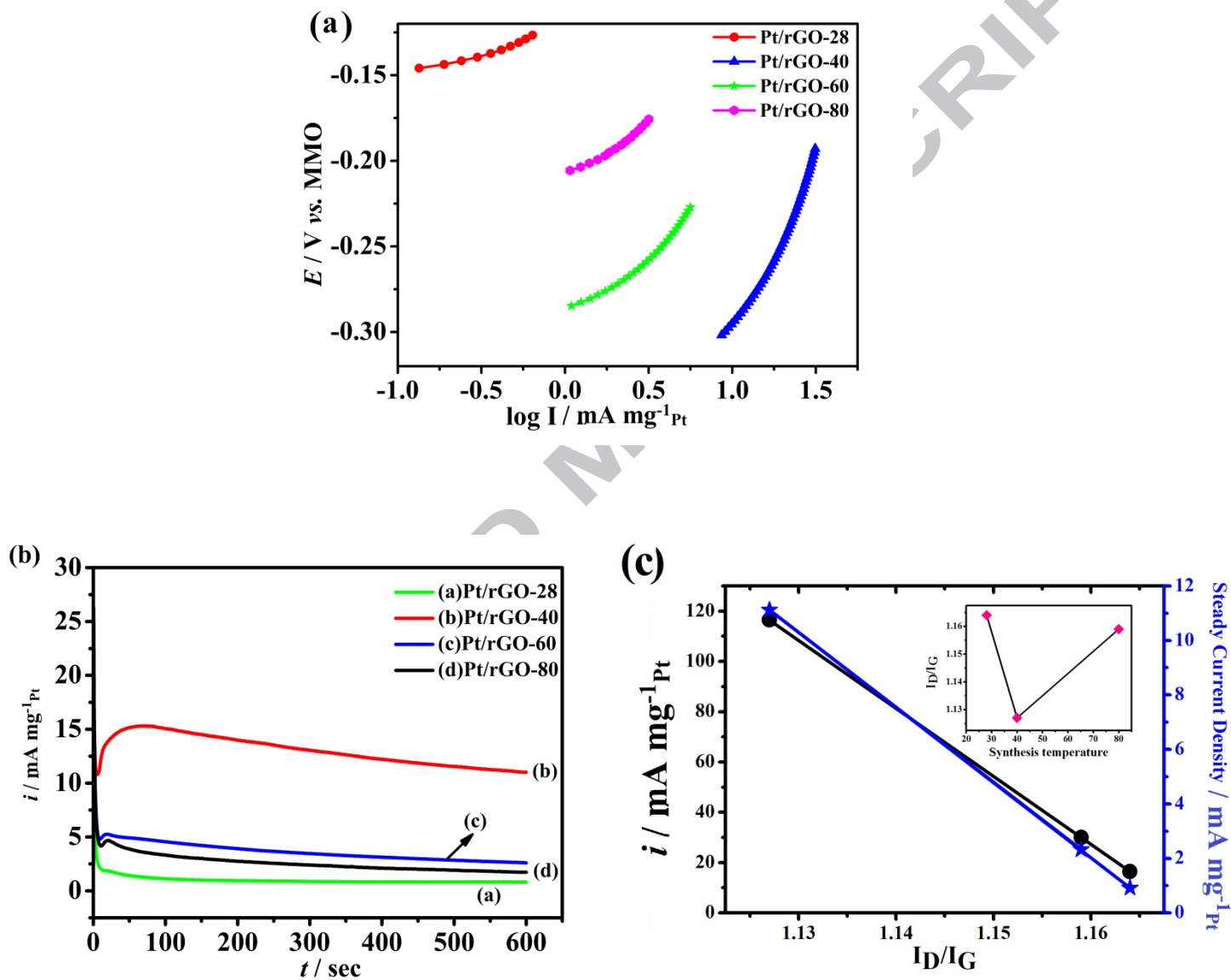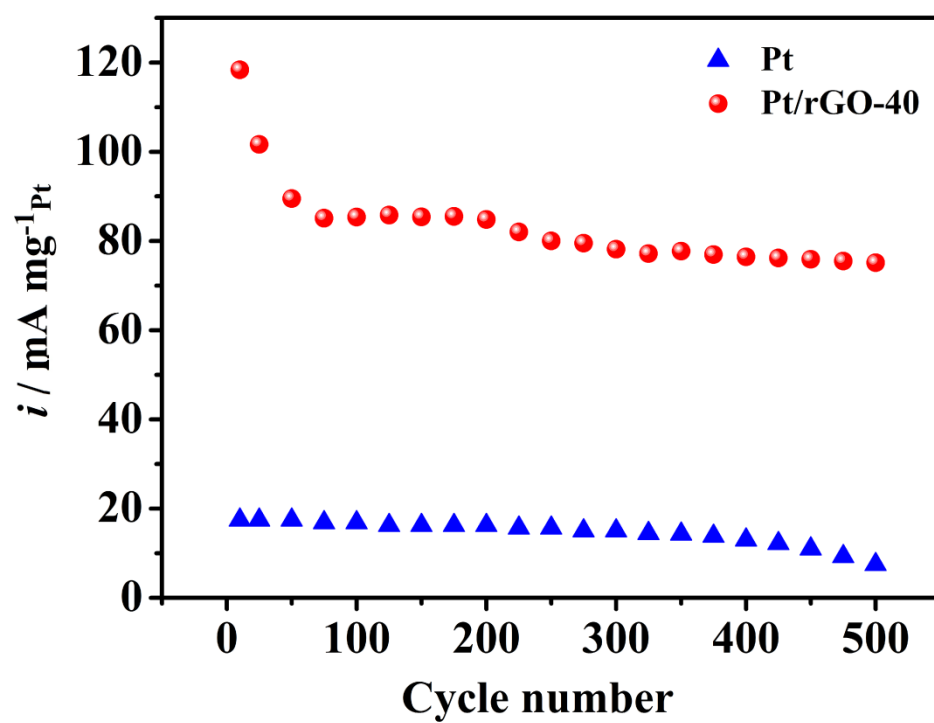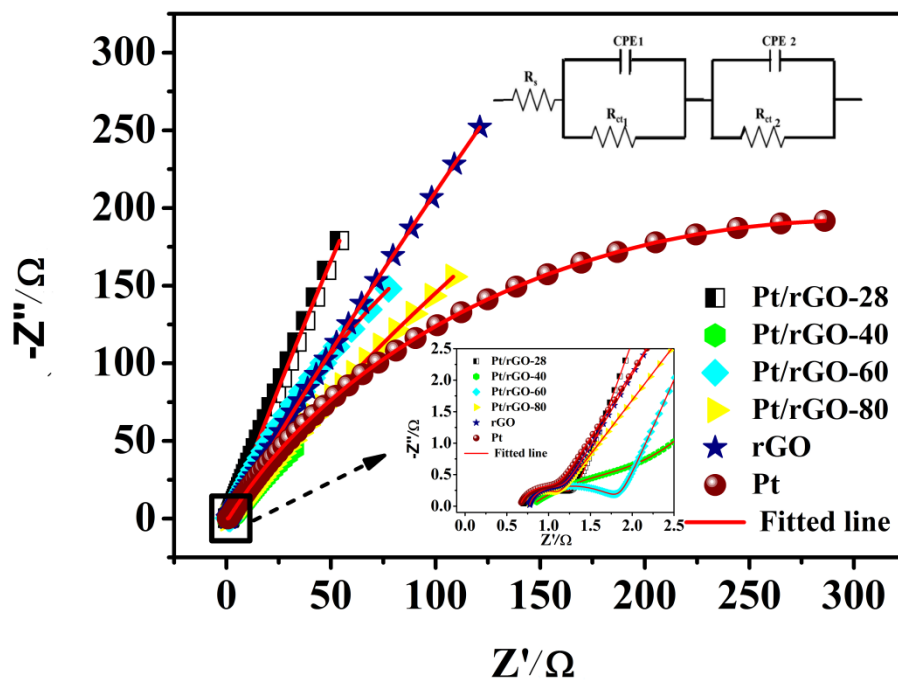**Figure 11**

Highlights

- ➤ Temperature controlled synthesis of Pt/rGO nanocomposites for alkaline oxidation of methanol.
- ➤ Poison tolerance capability depends on defect concentration which increases with temperature.
- ➤ Smaller Pt nanoparticle in the vicinity of sp^2 C-OH on rGO is suitable for better electrocatalysis.

Conflicts of interest:

The authors declare no conflicts of interest.